

Article

Silver Nanoparticles: An Instantaneous Solution for Anticancer Activity against Human Liver (HepG2) and Breast (MCF-7) Cancer Cells

Abdulaziz A. Al-Khedhairy ^{1,*} and Rizwan Wahab ² ¹ Zoology Department, College of Science, King Saud University, Riyadh 11451, Saudi Arabia² Chair for DNA Research, Zoology Department, College of Science, King Saud University, Riyadh 11451, Saudi Arabia; rwahab@ksu.edu.sa* Correspondence: kedhairi@ksu.edu.sa

Abstract: Cancer is a cataclysmic disease that affects not only the target organ, but also the whole body. Metal-based nanoparticles (NPs) have recently emerged as a better option for the treatment of this deadly disease. Accordingly, the present work describes a means to control the growth of cancer cells by using colloidal silver nanoparticles (AgNPs) processed via homemade solutions and the characterization of these materials. The AgNPs may become an instantaneous solution for the treatment of these deadly diseases and to minimize or remove these problems. The AgNPs exhibit excellent control of the growth rate of human liver (HepG2) and breast (MCF-7) cancer cells, even at a very low concentrations. The cytotoxic effects of AgNPs on HepG2 and MCF-7 cancer cells were dose dependent (2–200 µg/mL), as evaluated using MTT and NRU assays. The production of reactive oxygen species (ROS) was increased by 136% and 142% in HepG2 and MCF-7 cells treated with AgNPs, respectively. The quantitative polymerase chain reaction (qPCR) data for both cell types (HepG2 and MCF-7) after exposure to AgNPs showed up- and downregulation of the expression of apoptotic (p53, Bax, caspase-3) and anti-apoptotic (Bcl2) genes; moreover, their roles were described. This work shows that NPs were successfully prepared and controlled the growth of both types of cancer cells.

Keywords: silver nanoparticles; cancer cells; MTT; NRU; ROS; qPCR

Citation: Al-Khedhairy, A.A.; Wahab, R. Silver Nanoparticles: An Instantaneous Solution for Anticancer Activity against Human Liver (HepG2) and Breast (MCF-7) Cancer Cells. *Metals* **2022**, *12*, 148. <https://doi.org/10.3390/met12010148>

Academic Editors: Manuel Aureliano, Nadiia I. Gumerova and Annette Rompel

Received: 6 December 2021

Accepted: 4 January 2022

Published: 14 January 2022

Publisher's Note: MDPI stays neutral with regard to jurisdictional claims in published maps and institutional affiliations.



Copyright: © 2022 by the authors. Licensee MDPI, Basel, Switzerland. This article is an open access article distributed under the terms and conditions of the Creative Commons Attribution (CC BY) license (<https://creativecommons.org/licenses/by/4.0/>).

1. Introduction

Cancer is a very complex disease; it affects not only specific organs, but also deregulates the whole body [1,2]. The uncontrolled progression of normal cells leads to the development of cancer [1,2]. Several factors are responsible for the growth of cancer cells, such as the accumulation of mutations in genes, deregulation of the signaling pathways, insensitivity to anti-growth signals, evasion of apoptosis, unlimited replicative potential, sustained angiogenesis, capacity to invade surrounding tissues, and the initiation of the acquisition of self-sufficient growth signals [3–5]. To date, many different types of cancers have been identified based on the cells present in the body, such as breast cancer, brain cancer, cervical cancer, colon cancer, kidney cancer, liver cancer, lung cancer, melanoma skin cancer, myeloma, skin cancer (non-melanoma), ovarian cancer, prostate cancer, stomach cancer, and vaginal cancer [6–12]. Liver and breast cancers are very common throughout the world [4]. The liver is the largest metabolic organ in the body and performs numerous functions, such as the removal of waste products (toxins) by the formation of harmless bile, and the production of important proteins and chemical substances that are required for the body to work normally [13]. Both developed and developing countries are greatly affected by the occurrence of such diseases. Hepatocellular carcinoma, a type of liver cancer, is the fourth most common malignant tumor in the world [14,15]. In 2018, there were 10,518 cancer deaths and 24,485 new cancer cases in Saudi Arabia, which has a

population of 33,554,333 [16]. However, in 2020, the number of deaths increased to 13,069 and a further 27,885 new cases were diagnosed, despite a relatively small population increase (34,813,867 individuals) [17]. This deadly disease is prevalent in many countries, for example, the USA the UK, Japan, and China [18,19]. In China, the mortality rate associated with this disease is the second highest of all tumors [14,15]. Every year in the United States, ~24,500 men and 10,000 women are diagnosed with liver cancer, and ~18,600 men and 9000 women die from the disease [18]. Similarly, another common cancer is breast cancer, most often reported in women [4]. More than one million women worldwide are estimated to be affected by breast cancer. The statistics for this disease vary extensively: in 2008, ~421,000 cases were recovered, whereas in 2009–2010, ~49,500 women were diagnosed with breast cancer in Europe and 230,480 cases were diagnosed in 2011 in USA [4]. The estimated number of cases of breast cancer is increasing daily. About ~268,600 cases were identified in women, but it is also detected in men (~2670 cases) in 2019; in 2020, ~42,170 women were diagnosed in the US and predicted to die [4]. According to a report on the incidence of cancer in 2010 in Saudi Arabia, the total number of cancer cases reported (SCR) was 13,706. Overall, the incidence of cancer was higher in women than in men. Cancer affected 6579 (48%) males and 7127 (52%) females [12]. Breast cancer, which originates from breast cells, affects both males and females, but the incidence is lower in males. Amongst females, breast cancer was the most common cancer, with 5378 newly diagnosed cases in 2010, accounting for 27.4% of all cases [20]. In 2020, 2.3 million women were diagnosed with cancer worldwide, and 685,000 deaths occurred. Amongst females, breast cancer accounts for one in four cancer cases and for one in six cancer deaths [21]. Breast cancer is one of the main causes of mortality in younger women and its incidence is increasing [22]. The occurrence of other cancers was lower: colorectal (11.1%), thyroid (7.4%), NHL (7.0%), liver (5.1%), leukemia (4.3%), lung (4.3%), skin (3.4%), stomach (3.1%), prostate (3.0%). The occurrence of breast cancer is much higher than any of these other types of cancer [20]. To eradicate the cancer from the body, various therapies have been tested, such as chemotherapy [23], hormone therapy [24], radiotherapy [25], immunotherapy [26], stem cell therapy [27], proton beam therapy [28], clinical trials [29], and cryoablation [30], etc. Surgery is also an option to remove the cancer cells from a specific organ in the body [31]. Although there are different treatment methods, these options are not affordable for the middle class and low-income or deprived families. To solve this problem, nanotechnology has been used to provide cancer therapy at a low cost, offering high efficacy against cancer cells without any harm to body systems [10,32]. To contribute to this solution, numerous types of metal and metal oxide nanostructures (MONs) have been prepared and utilized, and metal nanoparticles (MNPs) can be easily produced via a solution process [10,32]. MNPs, for example gold, platinum, rubidium, and selenium, are more expensive than AgNPs [33–35]. AgNPs can be prepared by facile, low-cost preparation methods and exhibit extraordinary properties with regard to optoelectronics [36], energy storage [37,38], ceramics [39], and surface-enhanced raman spectroscopy (SERS) [40]. In addition, owing to their physiochemical properties, AgNPs are also applied for biological activities, such as drug delivery, photodynamics [41], imaging [42], gene therapy [43], and antibacterial, anti-microbial, and anticancer agents [44,45]. AgNP-induced antibacterial activity has been reported to include adhesion to microbial cells, dispersion inside the cells, free radical/ROS generation, and the modulation of microbial signal transduction pathways [46]. The anticancer activity of AgNPs has been reported through the accumulation of AgNPs in the mitochondria and nucleus, where they interact with DNA. Further oxidative stress and mitochondrial damage can activate cancer cell death through via apoptosis [47]. AgNPs also have unique catalytic properties, enhanced electrical conductivity [48], and greater chemical stability [49]. Among various noble metals, the nanometer-scale AgNPs and their related nanocomposites, such as silver-reduced graphene oxide nanocomposites (Ag/RGO NCs), and doped materials, are an excellent option owing to their enhanced eco-friendly properties, including their non-toxic effects in numerous biological entities when applied at low concentrations [44,50,51].

Due to their broad applicability, it is necessary to produce AgNPs at a very low cost and through a simple easy process. Accordingly, the current work discussed the synthesis of AgNPs. The AgNPs were synthesized by a solution process at low temperature ($\sim 50^\circ\text{C}$) in a very short period and were well characterized. Despite the various applications of AgNPs, very limited studies are available on their effects on cancer cell growth, cytotoxicity, and gene expression when administered at low concentrations. The available literature shows that the AgNPs are usually prepared either with various complex materials or by green processes that require a longer preparation time and high costs [52–55]. In addition, these processes do not achieve strong cytotoxic activities at low concentrations. Therefore, the core objective of the current work was to elucidate the effect of AgNPs in human liver (HepG2) and breast (MCF-7) cancer cells. Metabolic disturbances affecting the viability of cells were examined using the MTT assay. Lysosomal toxicity was quantitated by neutral red uptake assay (NRU). Transcriptional changes in apoptotic genes were measured by qPCR study. The novelty of the present work is the synthesis of AgNPs by a very low-cost chemical method, which was the main objective of the present work, and their application to liver (HepG2) and breast (MCF-7) cancer cells.

2. Materials and Methods

2.1. Materials

2.1.1. Reagents and Consumables for the Biological Study

Chemicals and consumable used for this experiment, such as MTT [3-(4, 5-dimethylthiazol-2-yl)-2, 5 diphenyltetrazolium bromide], were procured from Sigma Chem. Co., Saint Louis, MO, USA, and applied to the cells without any modification except dilution. Further, Dulbecco's Modified Eagle Medium (DMEM) and MEM, used for culture medium, antibiotics–antimycotics, and FBS were bought from Invitrogen, Waltham, MA, USA. The plastic ware and other related consumables products for cell culture were purchased from Nunc, Roskilde, Denmark.

2.1.2. Methods

Synthesis of Silver Nanoparticles (AgNPs)

The synthesis of AgNPs was achieved via a solution process by using silver nitrate (AgNO_3), which acts as a precursor material for the formation of NPs, whereas trisodium citrate salt was employed as a reducing agent. The chemicals required for the formation of NPs were acquired from Sigma Aldrich Chem. Co, Saint Louis, MO, USA. In the experiment, a minute quantity of silver nitrate (AgNO_3 , 0.008 M, ~ 0.06792 g) was dissolved in ~ 49 mL of double-distilled water (DDW) in a 100 mL capacity beaker at room temperature and ~ 1 mL of sodium citrate ($\text{N}_3\text{C}_6\text{H}_5\text{O}_7$, ~ 3 mM) was added slowly to this solution to reduce the silver ions (Ag^+) in the silver nitrate solution [44]. The colorless solution of silver nitrate changed to a white solution after the sodium citrate was added. The solution turned brown within few seconds (s) and then to black, but for the complete reaction it was transferred to a dark chamber and covered with aluminum foil. The solution was kept for ~ 45 min at 50°C until the color change from brown to black was complete ($\text{pH} = 6.97$), demonstrating the creation of AgNPs in the solution. The black-colored silver particles were pelleted through centrifugation (3000 rpm for 3 min, Eppendorf, 5430R, Centrifuge, Hamburg, Germany). The obtained black-colored silver particles settled at the bottom of centrifuge tube and were washed with the organic solvent methanol (MeOH, 2–3 times) to eliminate the ionic impurities from the solution. The product was dried and stored for further elucidation of structural and chemical properties.

Material Characterization

X-ray diffraction (XRD) (Rigaku, Tokyo, Japan) was used to determine the crystallinity, particle size, and phases of the prepared black powder sample. The samples were analyzed between 20 and 85° with using $\text{Cu}_{\text{K}\alpha}$ source ($\lambda = 1.54178 \text{ \AA}$) at a rotation speed of $6^\circ/\text{min}$ with an accelerating voltage of 40 kV and current of 40 mA (Rigaku, Tokyo, Japan). The

structural assessment of powder sample was performed using SEM (JEOL 6380, JSM, Tokyo, Japan) with a scanning resolution speed of 1.0 nm at 5 kV with low (30,000 \times) and high magnification (50,000 \times). To perform scanning electron microscopy (SEM), the black-colored powder sample was sprinkled on carbon tape on the sample holder, fixed, and analyzed at room temperature. Concurrently, transmission electron microscopy (TEM, JEOL JEM-2010, Tokyo, Japan at 100 kV) was also used to confirm the structural details of prepared product. For the TEM analysis, a very small amount of powder was dissolved in ethanol (EtOH) and sonicated for ~15 min. A copper grid (~400 mesh, Sigma Aldrich, Saint Louis, MO, USA) was dipped to this sonicated powder sample for 2–3 s, and dried at room temperature. Once the grid was completely dry, it was placed on a sample holder and analyzed at 100 kV at room temperature. The chemical fingerprint of the black powder was also investigated using FTIR spectroscopy (Perkin Elmer-FTIR Spectrum-100, Shelton, WA, USA) within range of 400–4000 cm^{-1} in KBr pellets. The optical characteristics of the processed powder were also determined by UV–visible spectroscopy (UV–vis, Shimadzu, Kyoto, Japan) in the range of 300–700 nm.

2.2. Cell Culture (HepG2, MCF-7 Cells) and Treatment with AgNPs

The liver (HepG2) and breast (MCF-7) cancer cells were procured from the ATCC and inoculated in medium (DMEM) with 10% fetal bovine serum (FBS), 0.2% sodium bicarbonate, and antibiotic–antimycotic solution (100 \times , 1 mL/100 mL) in a CO₂ incubator (5% CO₂ & 95% humidity) at 37 °C. Before the experiments, the cell viability was assessed by trypan blue dye as per the protocol [56] and 95% cell viability was achieved for the study. We used cells between passages 10 to 12 passages for treatment with the prepared nanomaterials. Serial dilution of AgNPs was performed to obtain the desired concentrations for exposure. The cells were seeded in 6-well or 96-well plates according to the experimental need. In this study, we selected MCF-7 and HepG2 cell lines because they have been proven to be a good in vitro model system to evaluate the cytotoxic activities of different nanoparticles [57,58].

2.3. MTT Assay

The viability of liver (HepG2) and breast (MCF-7) cancer cells treated with AgNPs and without treatment (control) was assessed using the MTT assay as per the following protocol [56,59]. For this experiment, initially, the cells were seeded in specialized 96-well plates (rate of 1×10^4 /well) for 24 h at 37 °C in a humidified environment. Afterwards, the cells were treated with AgNPs at 2, 5, 10, 25, 50, 100, and 200 $\mu\text{g}/\text{mL}$ and kept in an incubator for 24 h. After the cancer cells were well mixed in the plates, a prepared stock solution of MTT (5 mg/mL in PBS) was added at 10 $\mu\text{L}/\text{well}$ in 100 μL of cell suspension and the plates were incubated for 4 h. When the incubation period was complete, the solution was removed from the wells and 200 μL of DMSO was added and mixed gently to dissolve the formazan product. The optical characteristics of the solution were examined at 550 nm using microplate reader (Multiskan Ex, Thermo Scientific, Vantaa, Finland). Control cells were also employed as a reference and run under the same conditions. Cell viability was calculated as per the equation mentioned below:

$$\% \text{ viability} = [(\text{mean absorbance of treated group})/(\text{mean absorbance of control group})] \times 100$$

2.4. NRU Assay

Lysosomal cytotoxicity assessment was also quantitated with and without AgNPs exposure via the neutral red uptake (NRU) assay as per the previously described protocol [60,61]. HepG2 and MCF-7 cells (1×10^4 /well) were seeded in specific 96-well plates. Afterwards, the cells were treated with the desired concentrations (2, 5, 10, 25, 50, 100, and 200 $\mu\text{g}/\text{mL}$) of AgNPs and kept for 24 h in an incubator. After exposure, the cancer cells were further incubated in NR medium (50 $\mu\text{g}/\text{mL}$) for 3 h. Later, the cells were washed

and the dye was extracted in 1% acetic acid and 50% ethanol solution and the color was read at 550 nm.

2.5. Reactive Oxygen Species (ROS)

ROS was also measured by using 2, 7-dichlorodihydrofluorescein diacetate (DCFH-DA) (Sigma Aldrich, Saint Louis, MO, USA) dye as a fluorescence agent, as per the previously described method [62]. The grown cells were treated with AgNPs for 24 h and thereafter, the cells were washed with PBS and further cultured for 30 min in DCFH-DA (20 μ M) in the dark at 37 °C before the cells were examined by using fluorescence microscope.

2.6. RNA Isolation and Quantitative Polymerase Chain Reaction (qPCR)

For qPCR analysis, RNA was extracted from HepG2 and MCF-7 cells (both control cells and cells treated with AgNPs at 25 μ g/mL for 24 h). The RNA was extracted using the RNeasy mini Kit (Qiagen) according to manufacturer's protocol. The purity of RNA was determined by a Nanodrop 8000 spectrophotometer (Thermo Scientific, Waltham, MA, USA). The cDNA was synthesized from treated and untreated cells by taking 1 μ g of RNA by Reverse Transcriptase kit using MLV reverse transcriptase (GE Healthcare, Chalfont Saint Giles, UK) as per the manufacturer's protocol. Gene expression analysis was performed with LightCycler[®] 480 SYBR Green I Master on a real-time PCR (LightCycler[®] 480, Roche Diagnostics, Rotkreuz, Switzerland). The final 20 μ L PCR reaction mixture contained 1 \times qPCR Green Master, 100 ng of the cDNA, and both the forward and reverse primers. The primers were used for the amplification were: GAPDH F-5' CCACTCCTCCACCTTTGAC3', R-5' ACCCTGTTGCTGTAG CCA3', Caspase-3 F-5' ACATGGCGTGTGCATAAAATACC3' R-5' CACAAAGCGACTGGATGAAC3', p53 F-5' CCCAGCCAAAGAAGAAACCA3', R-5' TTCCAA GGCCT CATT CAGCT3', Bax F-5' TGCTTCAGGGTTTCATCCAG3', R-5' GGCGGCAATCATCTCTG3', Bcl-2 5' AGGAAGTGAACATTCGGTGAC3' R-3' 5'GCTC AGTTCCAGGACCAGGC3'. The GAPDH gene was used as an internal housekeeping control to normalize the expression levels of p53, caspase 3, bax, and bcl2. The cycling conditions were used for amplification: heat-denaturing step at 95 °C for 10 min in the first step, then 45 cycles each at 95 °C for 20 s, annealing at 58 °C for 20 s, and the elongation period at 72 °C for 20 s. qPCR was performed in triplicate. All data are expressed as the mean of three independent experiments, calculated by the 2- $\Delta\Delta$ CT method.

2.7. Statistical Analysis

The obtained data are displayed as the mean \pm SD and the statistical analysis was performed by Student's *t*-test. Results were considered significant when $p < 0.05$.

3. Results

3.1. X-ray Diffraction Pattern (XRD)

Figure 1 shows the X-ray diffraction pattern (XRD) of the processed powder via solution process. The XRD was utilized to determine the crystallinity, crystallite size, and phases of the prepared powder material. The spectrum illustrates the indexed and assigned peaks with their related positions, such as <111>(38.03), <200>(44.17), <220>(64.29), <311>(77.19), and <222>(81.30), and their close relation to the face-centered cubic (FCC) structure of metallic silver with the lattice constant $a = 0.4086$ nm, analogous to the accessible standards data of Joint Committee on Powder Diffraction Standards (JCPDS card no. 04-0783) (Figure 1) and earlier published literature [39,44]. The extreme peak positions indicate that the black-colored powder formed exhibits high crystallinity and a small particle size. The crystallite size was calculated by using the Scherrer formula with Origin software, as described previously, which was found to be \sim 13 nm (Table 1) [39,44]. The XRD spectrum displayed only Ag peaks, without any other chemical impurities, further indicating the purity of the sample.

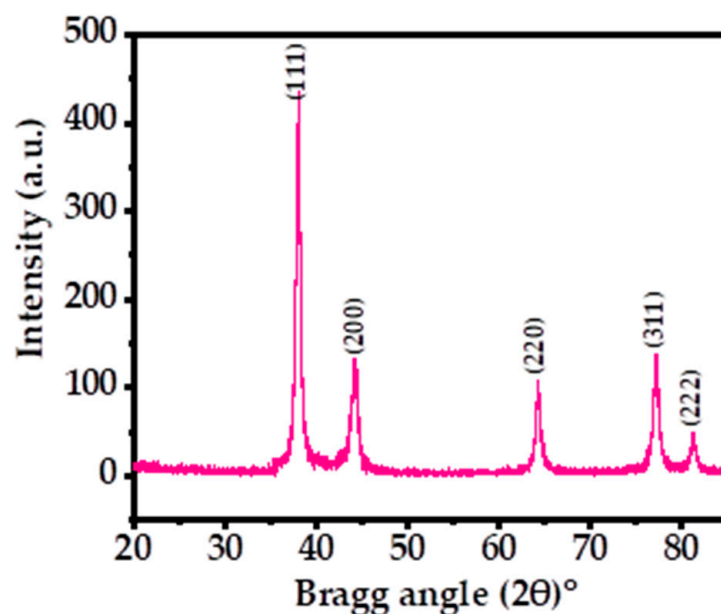


Figure 1. XRD patterns of the processed silver nanoparticles (AgNPs) showing the corresponding peaks.

Table 1. Calculation of crystallite size and the phases of AgNPs powder.

S.N.	Phases	Peak Positions	FWHM	Crystallite Size D (nm)	D nm (Average Size)	Final Particle Size (nm)
1.	111	38.038	0.661	12.712	12.267	13.166 nm
2.	200	44.173	1.020	8.398	12.156	-
3.	220	64.296	0.713	13.163	13.408	-
4.	311	77.196	0.809	12.564	13.531	-
5.	222	81.308	0.722	14.498	14.498	-

3.2. Morphological, Chemical, and Optical Analysis of AgNPs

The morphological assessment of AgNPs was performed for the prepared powder using scanning electron microscopy (SEM) and the obtained images are shown in Figure 2. The low-magnification image of AgNPs captured at $30,000\times$ resolution shows that small spherical nanostructures were scattered about the whole surface (Figure 2A). The NPs were well arranged and it appeared that these NPs were linked with other particles and formed spherical structures. A high-magnification image at $50,000\times$ resolution was captured and is presented here to provide further confirmation of the individual particle shape and size (Figure 2B). From the obtained data, the estimated diameter of each individual particle was in the range of $\sim 13 \pm 1$ nm. The SEM analysis was in good agreement and consistent with the above XRD data.

For more accurate observations, the black-colored powder was also analyzed by TEM, as described above, and the data are presented in Figure 3A. Several nanometer (nm)-size particles (NPs) were present in the obtained image, which showed individual NPs as $\sim 13 \pm 1$ nm in size (Figure 3B). The TEM images confirmed that the spherical NPs surfaces were smooth and clear, consistent with the SEM data.

Figure 4A shows the obtained signals at 3434 , 1589 , 1384 , 1115 , and 619 cm^{-1} in the FTIR spectrum, which revealed the functional groups involved in the stabilization of AgNPs. The shallow band at 3434 cm^{-1} was correlated with the water molecule, whereas a sharp band at 1589 cm^{-1} was displayed, which originated from the band at 1685 cm^{-1} , confirming the presence of the O–H group. A sharp band at 1384 cm^{-1} and a very small band at 1115 cm^{-1} were the stretching and bending mode of vibration of NO_3^{2-} molecule.

The small shallow band presented at 619 cm^{-1} shows the presence of silver metal in the spectrum [39,44]. The FTIR results suggest that AgNPs were synthesized without the use of any additives or capping agents.

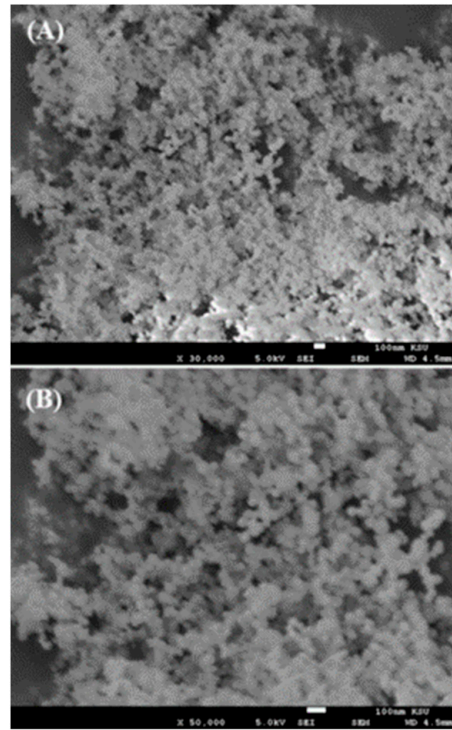


Figure 2. SEM images of AgNPs collected at (A) low magnification and (B) high magnification.

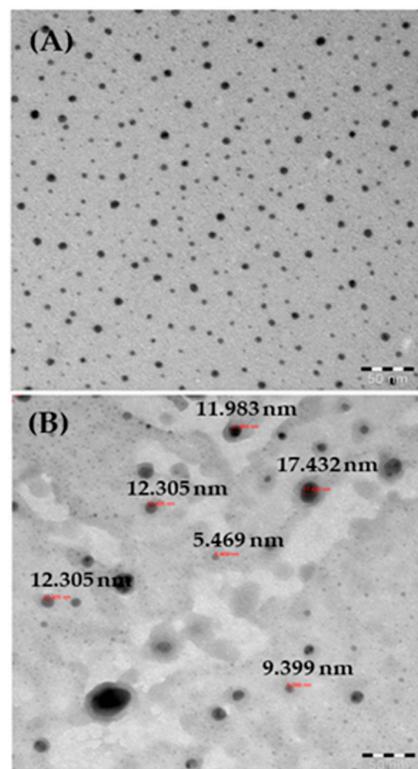


Figure 3. (A) TEM images of AgNPs; (B) measurements of individual particle sizes.

The optical properties of AgNPs were also analyzed via UV–vis spectroscopy at room-temperature, shown as in Figure 4B. A sharp peak was detected in the spectrum at 410 nm (Figure 4B), which was due the existence of Ag ions. No other peak was observed in the spectrum, which corroborated that the AgNPs possess excellent optical properties. Because of the higher band gap, the material is very efficient and optically active and exhibits good chemical and optical characteristics. The optical band gap energy (E_g) of the AgNPs can be calculated by using Tauc's equation [63], which exhibits the relationship between the absorption coefficient and the incident photon energy of material.

Tauc's equation is as follows:

$$\alpha hv = A(hv - E_g)^n$$

where α is the absorption coefficient, hv is the photon energy, A is a constant, E_g is the optical band gap, and n is a value that depends on the nature of the electronic transition responsible for the absorption ($n = \frac{1}{2}$ for direct transitions and $n = 2$ for indirect transitions). As per Tauc's equation, the calculated optical band gap of the AgNPs was found to be ~ 3.02 eV, analogous to previously published literature [63]. Because of the sufficient band gap, the material is efficient and optically active and exhibits good characteristics.

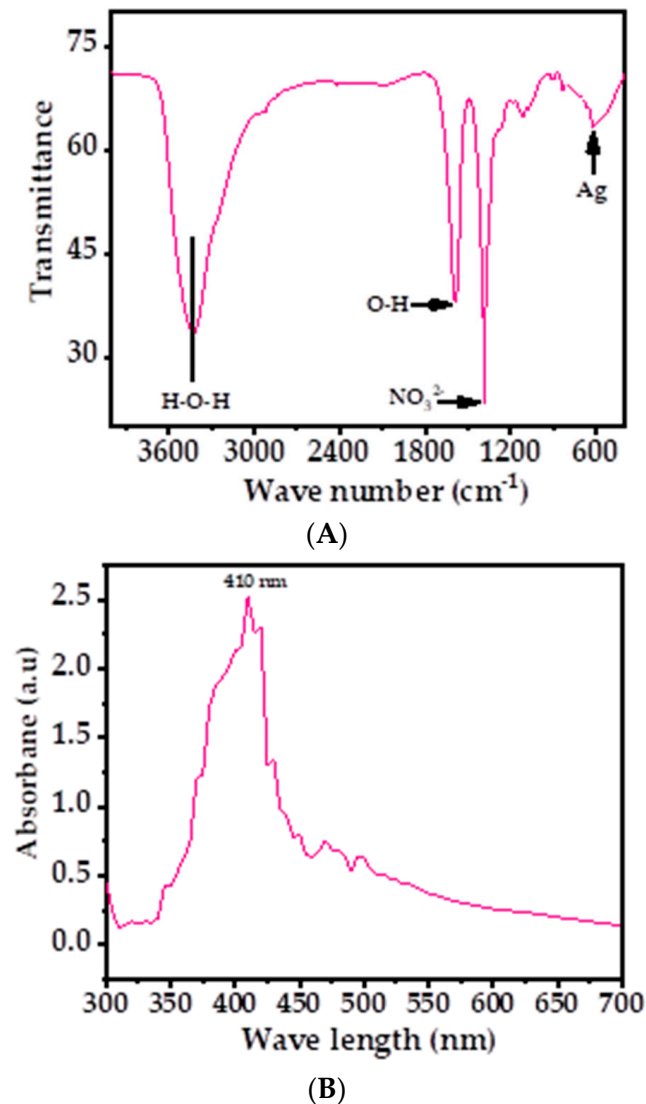


Figure 4. (A) FTIR spectrum of AgNPs depicts the corresponding functional groups; (B) the UV–visible spectrum of AgNPs.

3.3. Morphological Changes in HepG2 and MCF-7 Cells after AgNPs Exposure

The liver (HepG2) and breast (MCF-7) cancer cells were cultured and their morphology detail was observed via light microscopy after incubation for 24 h in the presence of varying concentrations (2, 5, 10, 25, 50, 100, and 200 $\mu\text{g}/\text{mL}$) of AgNPs (Figure 5). Representative images of both cell lines show no remarkable changes in the morphology at AgNP concentrations of 2–10 $\mu\text{g}/\text{mL}$. However, AgNPs at 25, 50, 100, and 200 $\mu\text{g}/\text{mL}$ affected the growth of cells and the rate was concentration and dose dependent. The morphology of cells at 50, 100, and 200 $\mu\text{g}/\text{mL}$ was greatly affected (Figure 5).

3.4. Cytotoxicity Induced by AgNPs

The cytotoxicity of AgNPs in both types of cancer cells (HepG2 and MCF-7) was measured via MTT assay. The viability of both cancer cells was reduced after their interaction with various concentrations (2, 5, 10, 25, 50, 100, and 200 $\mu\text{g}/\text{mL}$) of AgNPs. In HepG2 cells, after 24 h of incubation with 2, 5, 10, 25, 50, 100, and 200 $\mu\text{g}/\text{mL}$ AgNPs, the cell viability was quantitated as 105%, 72%, 19%, 18%, 18%, 18%, and 18% (Figure 6A), respectively. For MCF-7 cells, the viability after 24 h was observed as 101%, 104%, 50%, 10%, 9%, 9%, and 9% for concentrations of 2, 5, 10, 25, 50, 100, and 200 $\mu\text{g}/\text{mL}$, respectively (Figure 6B). The half-maximal inhibitory concentration (IC_{50}) values obtained for AgNPs against HepG2 and MCF-7 cells were 5.18 $\mu\text{g}/\text{mL}$ (Figure 7A) and 9.85 $\mu\text{g}/\text{mL}$ (Figure 7B), respectively, as determined by the MTT assay (Figure 7). A linear plot was also constructed with using three determinants for HepG2 (Figure 7A-inset) and MCF-7 cells (Figure 7B-inset) and the R^2 values were 0.89 and 0.63, respectively.

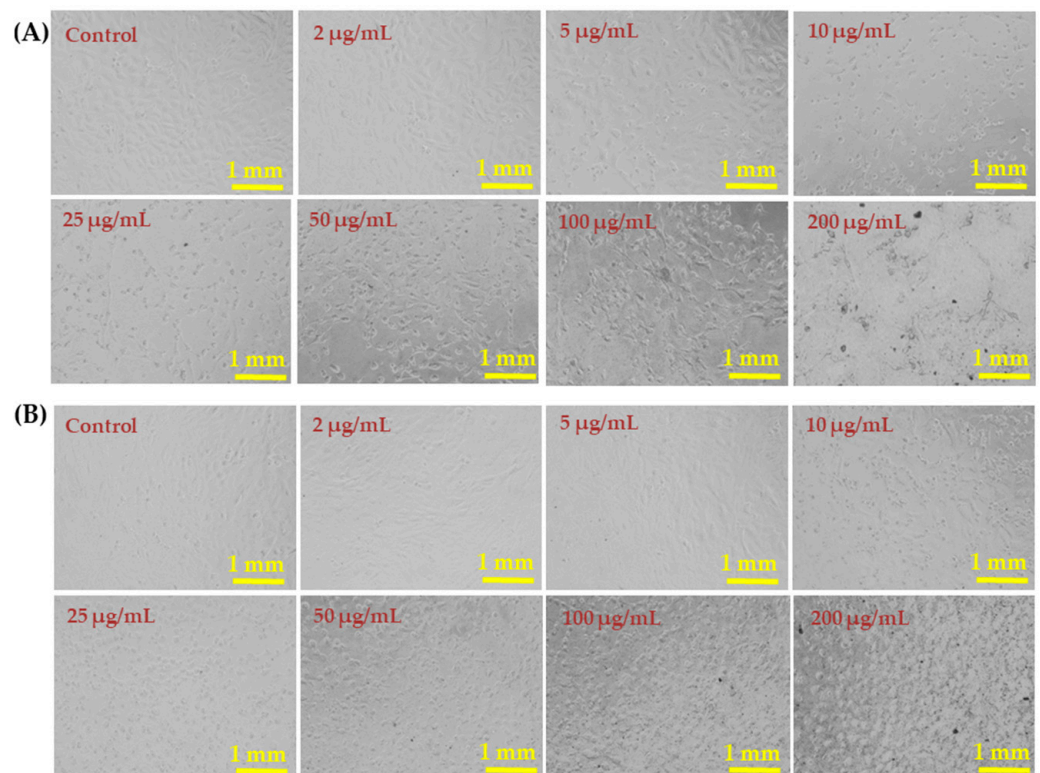


Figure 5. Morphological changes in HepG2 cells (A) and MCF-7 cells (B) exposed to AgNPs for 24 h. Cell images were taken under an inverted microscope at 20 \times magnification. Each scale bar = 1 mm.

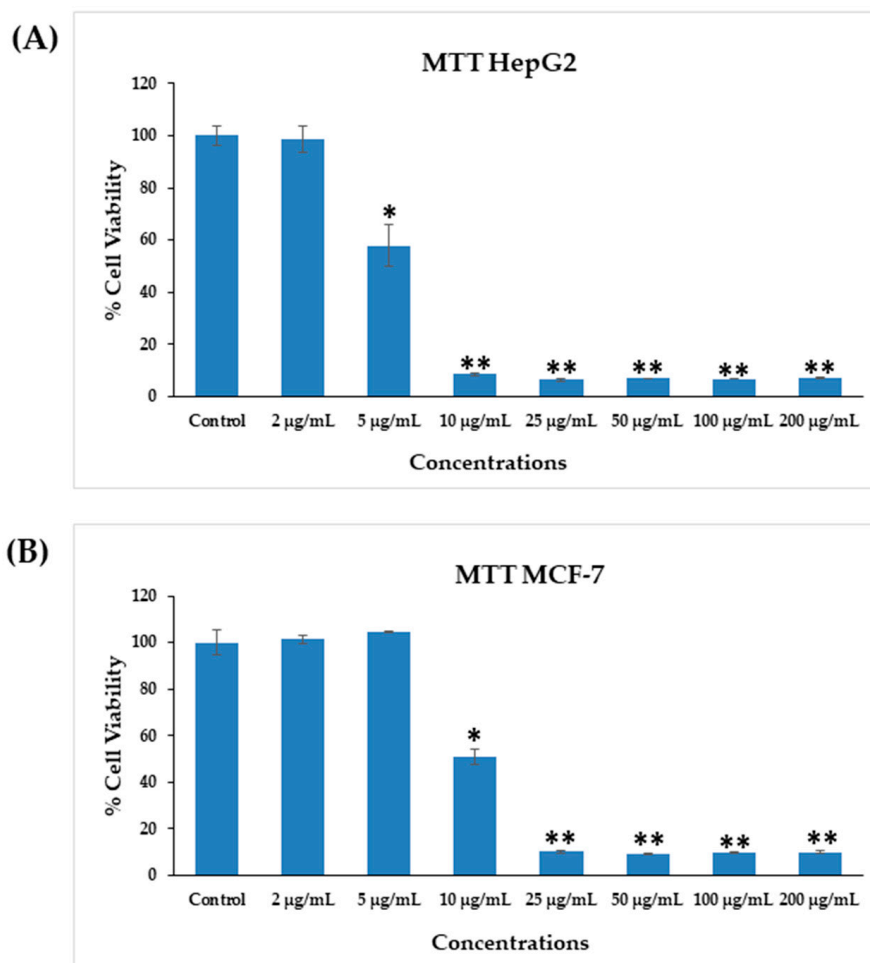


Figure 6. Cytotoxicity assessments by MTT assay in HepG2 cells (A) and MCF-7 cells (B) after exposure to AgNPs at different concentrations for 24 h. The values are mean \pm SE of three independent experiments. * $p < 0.05$, ** $p < 0.01$ vs. Control.

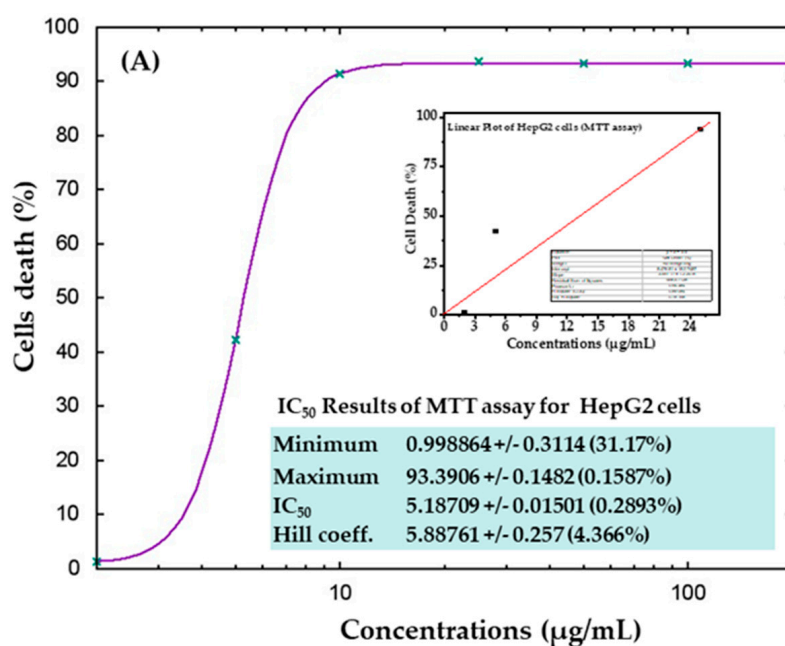


Figure 7. Cont.

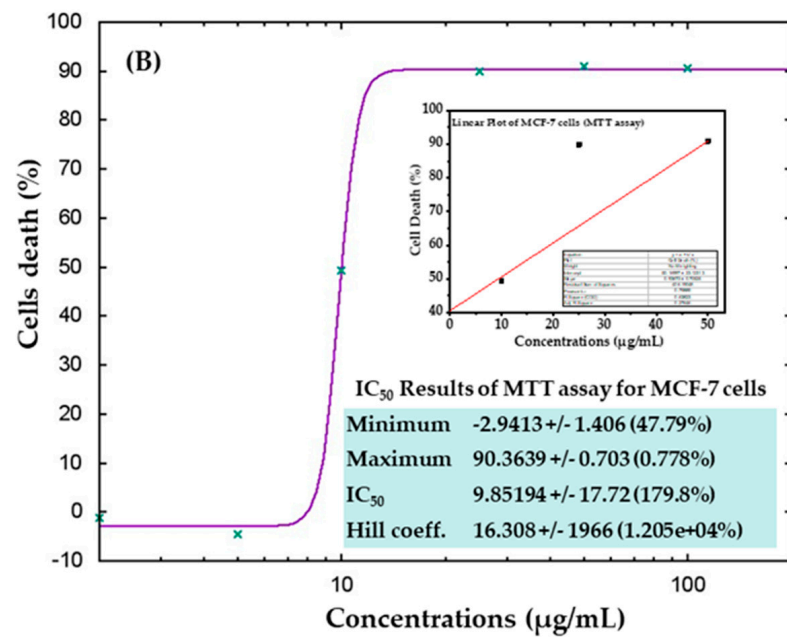


Figure 7. IC₅₀ result of MTT assay for HepG2 (A) and MCF-7 (B) cells with their corresponding linear plots of HepG2 (A-inset) and MCF-7 (B-inset) using three determinants respectively.

3.5. Cytotoxicity Study via NRU Assay in HepG2 and MCF-7 Cells after Exposure to AgNPs

The cytotoxic effects were also confirmed in control samples and samples treated with AgNPs via the NRU assay, as described in materials and methods. Similar trends were observed in the NRU assay for both cell types. The obtained data revealed that at the initial doses of AgNPs, the viability of cancer cells was not much affected; however, as the concentration increased, the survival of cells reduced dramatically. In HepG2 cells, cell viability quantitated by the NRU assay after 24 h was observed as 105%, 72%, 19%, 18%, 18%, 18%, and 18% for the concentrations of 2, 5, 10, 25, 50, 100, and 200 µg/mL, respectively (Figure 8A). In case of MCF-7 cells, the cell viability was recorded as 105%, 113%, 54%, 22%, 22%, 21%, and 21% for the concentrations of 2, 5, 10, 25, 50, 100, and 200 µg/mL, respectively (Figure 8B). The half-maximal inhibitory concentration (IC₅₀) values obtained for AgNPs against HepG2 and MCF-7 cells were 5.31 µg/mL (Figure 9A) and 9.69 µg/mL (Figure 9B), respectively, by NRU assay (Figure 9). A linear plot was also constructed using three determinants for HepG2 (Figure 9A-inset) and MCF-7 cells (Figure 9B-inset), and the R² values were 0.99 and 0.96, respectively.

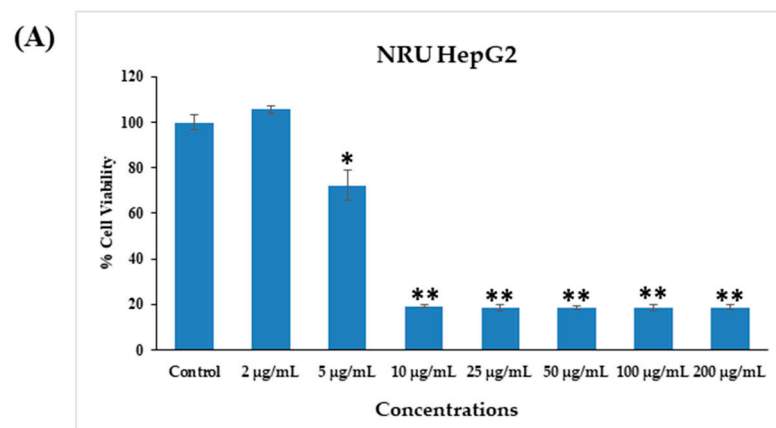


Figure 8. Cont.

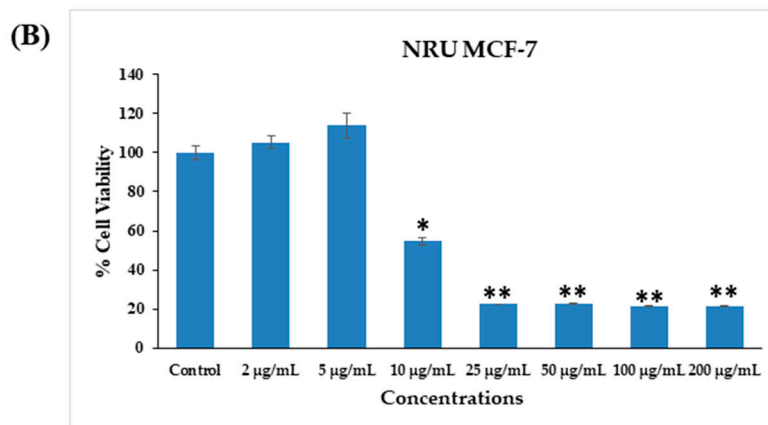


Figure 8. Cytotoxicity assessment by NRU assay in HepG2 (A) and MCF-7 (B) cells after exposure to different concentrations of AgNPs for 24 h. The values are the mean ± SE of three independent experiments. * $p < 0.05$, ** $p < 0.01$ vs. Control.

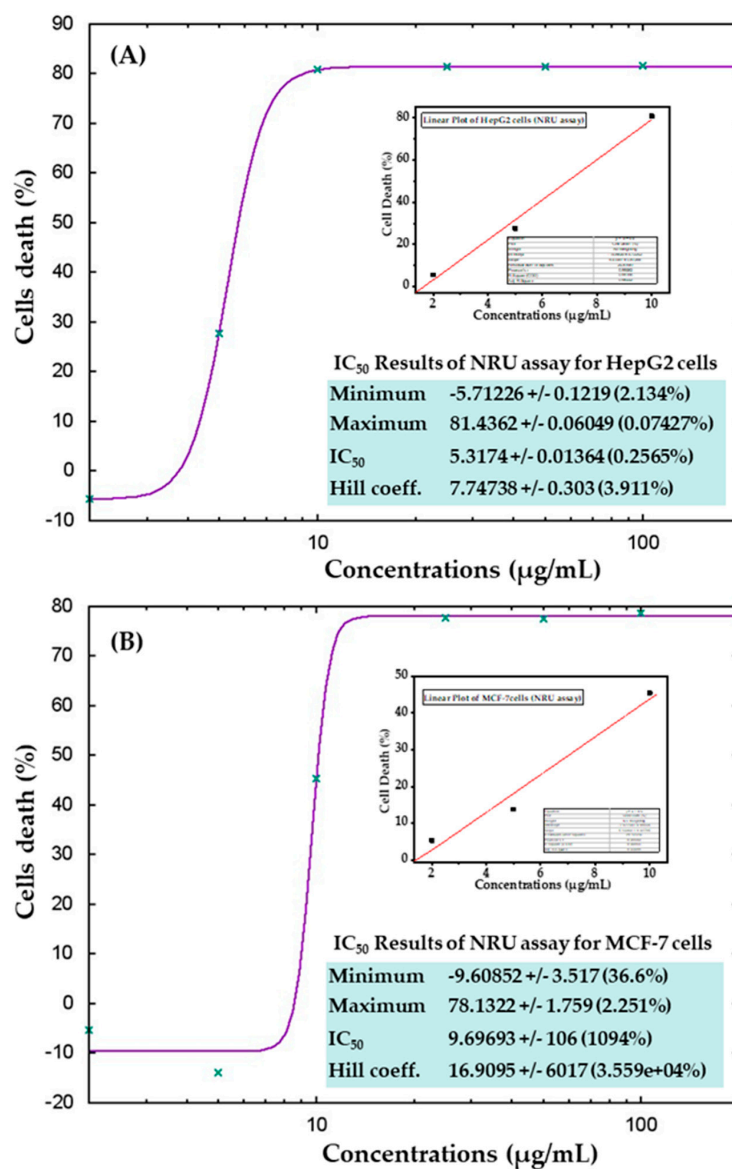


Figure 9. IC₅₀ values in the NRU assay for HepG2 (A) and MCF-7 (B) cells with the corresponding linear plots for HepG2 (A-inset) and MCF-7 (B-inset) using three determinants respectively.

3.6. ROS Generation in HepG2 and MCF-7 Cells after Exposure to AgNPs

Similar trends in ROS generation were observed in HepG2 and MCF-7 cells after exposure to AgNPs at 100 $\mu\text{g}/\text{mL}$ for 24 h (Figure 10). Compared with the control, the ROS level increased in both cell types after AgNPs exposure, as evident from the images (Figure 10A). At 25 $\mu\text{g}/\text{mL}$, ROS generation increased to 116 and 123% in HepG2 and MCF-7 cells, respectively, whereas at 50 $\mu\text{g}/\text{mL}$, ROS generation increased to 130 and 138% in HepG2 and MCF-7 cells, respectively. In addition, at a higher concentration (100 $\mu\text{g}/\text{mL}$), ROS generation increased to 136% and 142% in HepG2 and MCF-7 cells respectively, as compared to the controls (Figure 10B).

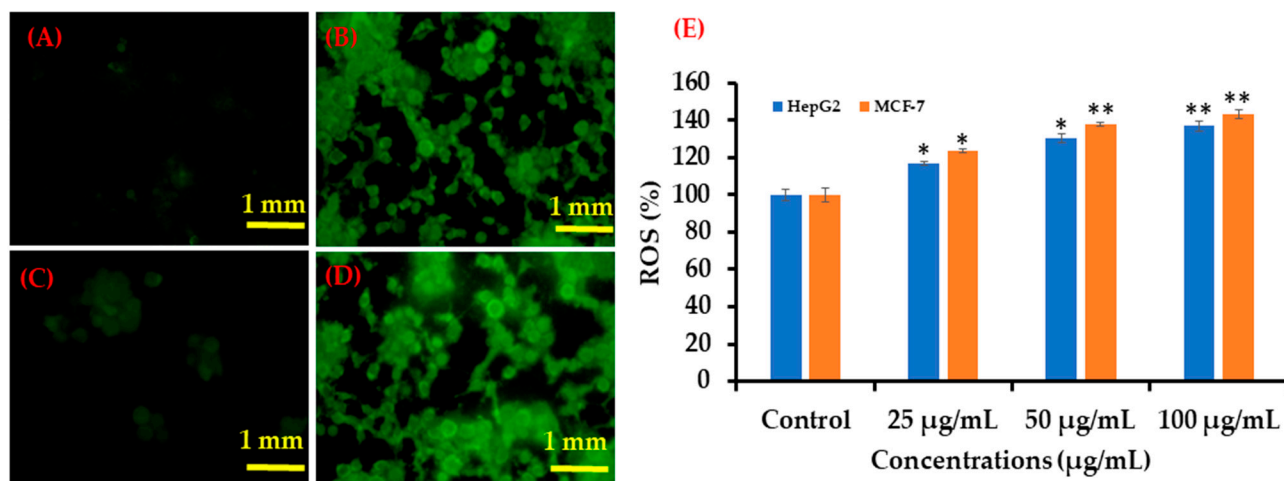


Figure 10. Green fluorescence showing ROS generation in HepG2 and MCF-7 cells after exposure to AgNPs. (A) Control (HepG2 cells), (B) 100 $\mu\text{g}/\text{mL}$ of NPs (HepG2 cells), (C) Control (MCF-7 cells) (D) 100 $\mu\text{g}/\text{mL}$ of AgNPs (MCF-7 cells), and (E) Bar diagram showing percentage change in ROS generation in HepG2 and MCF-7 cells exposed to 25–100 $\mu\text{g}/\text{mL}$ AgNPs. Each scale bar = 1 mm. * $p < 0.05$, ** $p < 0.01$ vs. Control.

3.7. mRNA Expression

The mRNA levels of apoptotic marker genes, such as p53, bax, caspase-3, and bcl2, in HepG2 and MCF-7 cells were examined by qPCR after exposure to AgNPs (25 $\mu\text{g}/\text{mL}$) for 24 h. The obtained results demonstrated notable alterations in apoptotic marker genes in HepG2 and MCF-7 cells (Figure 11). Relative to the control, in HepG2 cells, bax, p53, and caspase-3 was upregulated by 3.2, 2.9, and 1.9 fold, while bcl2 was downregulated by 0.70 fold (Figure 11A). A similar trend was also observed in MCF-7 cells, in which bax, p53, and caspase-3 were upregulated by 3.5, 3.0, and 2.8 fold, respectively, and bcl2 was downregulated by 0.50 fold (Figure 11B).

3.8. Discussion

Silver nanoparticles (AgNPs) exhibit unique and interesting properties, including notable physiological characteristics and broad applicability [64]. In this work, AgNPs were prepared via a solution process in a very short time, and were well characterized. Silver is an essential element that protects the body from microorganisms, and has the ability to easily conjugate to DNA, peptides, antibodies, and enzymes [65,66]. The synthesized AgNPs were utilized to treat HepG2 and MCF-7 cancer cells and their cytotoxic effects were examined through various means, such as MTT, NRU, ROS, and qPCR assays. The size, phases, and crystallinity of the processed material were assessed via XRD patterns. In addition, the morphology of the prepared black powder was examined via SEM and TEM, which revealed the spherical structured of the NPs. The spherical AgNPs were utilized to treat liver (HepG2) and breast (MCF-7) cancer cells and their effect on the proliferation of cells was examined. Previous reports showed that the cytotoxicity of cancer cells is

greatly affected and is responsible for the regulation of cancer cell growth [65,66]. Despite this, several other factors were also affected, such as the shape of the nanostructures, size, composition of cells, culture medium, doses of nanostructures, and pH [64,66]. The morphological changes after the interaction of different concentrations (2, 5, 10, 25, 50, 100 $\mu\text{L}/\text{mL}$) of AgNPs with cancer cells were observed using an inverted microscope after a 24 h incubation period, and cell death was observed. The AgNPs were determined to be very small in size (AgNPs $\sim 13 \pm 1$ nm), which allowed these NPs to enter easily into cells (unit size ~ 20 μm) and are responsible for the cell death [57,67,68]. Besides the other parameters affected the level of ROS was increased, which was responsible for the toxicological effects [69–71]. The gene expression (qPCR) data indicate the apoptotic cell death. The expression of the selected apoptotic markers genes, i.e., p53, bax, and caspase 3, was upregulated by AgNPs in both cell types [72,73]. The phenomenon of why AgNPs are able to destroy the cells and organelles to produce enzymatic changes requires further investigation, which will help to clarify utility of NPs in HepG2 and MCF-7 cancer cells [73]. The growth of HepG2 and MCF-7 cells was affected by doses of AgNPs. The previously published literature reveals that most studies used either they higher concentrations of nanostructures or complex chemical compounds, which are not appropriate for human body [73–76]. From our experiments, we believe that a minute quantity of the nanostructure is sufficient to achieve the control of cancer cell growth. AgNPs have a very small size in solution, allowing them to more easily target cellular organelles compared with other complex and organic-based drugs.

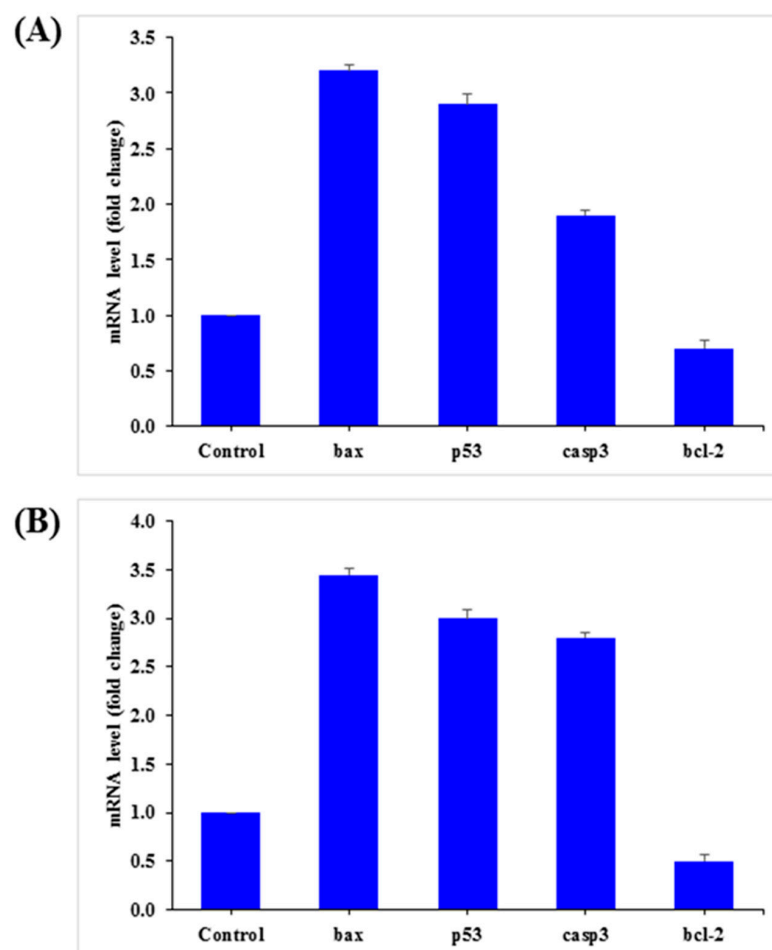


Figure 11. Quantification of mRNA fold-change of apoptotic genes (p53, bax, and casp3) and anti-apoptotic gene (Bcl2). HepG2 (A) and MCF-7 (B) cells treated with 25 $\mu\text{g}/\text{mL}$ of AgNPs for 24 h. For the internal control, GAPDH was used. The values are the mean \pm SE of three independent experiments. Statistically significant differences as compared to the control ($p < 0.05$).

4. Conclusions

In summary, the present study, AgNPs (size $\sim 13 \pm 1$ nm) were synthesized through a chemical solution method and their properties were characterized by XRD, SEM, TEM, FTIR and UV–vis methods. AgNPs were employed from very low (2 $\mu\text{g}/\text{mL}$) to high (200 $\mu\text{g}/\text{mL}$) concentrations to treat HepG2 and MCF-7 cancer cells, and the cytotoxic effects in HepG2 and MCF-7 cancer cells were dose-dependent. At the low doses (2–5 $\mu\text{g}/\text{mL}$ NPs), there were no changes in HepG2 and MCF-7 cells in terms of their morphology and growth, whereas at higher concentrations (10–200 $\mu\text{g}/\text{mL}$), the growth was strongly affected and the viability decreased to 10%. This work indicates the potential to apply AgNPs against both types of cancer cells and suggests they will be useful as a nanodrug. The current study shows that AgNPs induce cytotoxicity and apoptosis via the p53 and caspase pathways in cancer cells. Moreover, AgNPs also mediated ROS generation.

Author Contributions: Conceptualization, A.A.A.-K.; methodology, A.A.A.-K.; software, R.W.; validation, R.W.; formal analysis, R.W.; investigation, R.W.; resources, A.A.A.-K.; data curation, R.W.; writing—original draft preparation, A.A.A.-K.; writing—review and editing, A.A.A.-K.; visualization, A.A.A.-K.; supervision, A.A.A.-K.; project administration, A.A.A.-K.; funding acquisition, A.A.A.-K. All authors have read and agreed to the published version of the manuscript.

Funding: Abdulaziz A. Alkhedhairy would like to thank Zoology Department, College of Science and Scientific Council, King Saud University, Riyadh, Saudi Arabia for support of this work over Sabbatical Leave for the academic year 2021–2022.

Data Availability Statement: The data presented in this study are available on request. The data are not publicly available at this time due to some technical limitations.

Acknowledgments: Abdulaziz A. Alkhedhairy would like to thank Zoology Department, College of Science and Scientific Council, King Saud University, Riyadh, Saudi Arabia for support of this work over Sabbatical Leave for the academic year 2021–2022.

Conflicts of Interest: The author declares that they have no known competing or financial interests.

References

1. Bray, F.; Jemal, A.; Grey, N.; Ferlay, J.; Forman, D. Global cancer transitions according to the Human Development Index (2008–2030): A population-based study. *Lancet Oncol.* **2012**, *13*, 790–801. [[CrossRef](#)]
2. Elenbaas, B.; Spirio, L.; Koerner, F.; Fleming, M.D.; Zimonjic, D.B.; Donaher, J.L.; Popescu, N.C.; Hahn, W.C.; Weinberg, R.A. Human breast cancer cells generated by oncogenic transformation of primary mammary epithelial cells. *Genes Dev.* **2001**, *15*, 50–65. [[CrossRef](#)] [[PubMed](#)]
3. Vahrmeijer, A.L.; Hutteman, M.; van der Vorst, J.R.; van de Velde, C.J.H.; Frangioni, J.V. Image-guided cancer surgery using near-infrared fluorescence. *Nat. Rev. Clin. Oncol.* **2013**, *10*, 507–518. [[CrossRef](#)] [[PubMed](#)]
4. Nardin, S.; Mora, E.; Varughese, F.M.; Avanzo, F.D.; Vachanaram, A.R.; Rossi, V.; Saggia, C.; Rubinelli, S.; Gennari, A. Breast Cancer Survivorship, Quality of Life, and Late Toxicities. *Front. Oncol.* **2020**, *10*, 864. [[CrossRef](#)]
5. Sadikovic, B.; Al-Romaih, K.; Squire, J.A.; Zielenska, M. Cause and consequences of genetic and epigenetic alterations in human cancer. *Curr. Genom.* **2008**, *9*, 394–408. [[CrossRef](#)]
6. Khan, M.I.; Mohammad, A.; Patil, G.; Naqvi, S.A.H.; Chauhan, L.K.S.; Ahmad, I. Induction of ROS, mitochondrial damage and autophagy in lung epithelial cancer cells by iron oxide nanoparticles. *Biomaterials* **2012**, *33*, 1477–1488. [[CrossRef](#)] [[PubMed](#)]
7. Ahamed, M.; Akhtar, M.J.; Raja, M.; Ahmad, I.; Kaleem, M.; Siddiqui, J.; AlSalhi, M.S.; Alrokayan, S.A. ZnO nanorod-induced apoptosis in human alveolaradenocarcinoma cells via p53, survivin and bax/bcl-2 pathways: Role of oxidative stress. *Nanomed. Nanotechnol. Biol. Med.* **2011**, *7*, 904–913. [[CrossRef](#)]
8. Chen, N.; He, Y.; Su, Y.; Li, X.; Huang, Q.; Wang, H.; Zhang, X.; Tai, R.; Fan, C. The cytotoxicity of cadmium based quantum dots. *Biomaterials* **2012**, *33*, 1238–1244. [[CrossRef](#)]
9. Reddy, K.M.; Feris, K.; Bell, J.; Wingett, D.G.; Hanley, C.; Punnoose, A. Selective toxicity of zinc oxide nanoparticles to prokaryotic and eukaryotic systems. *Appl. Phys. Lett.* **2007**, *90*, 213902–2139023. [[CrossRef](#)]
10. Wahab, R.; Kaushik, N.K.; Kaushik, N.; Choi, E.H.; Umar, A.; Dwivedi, S.; Musarrat, J.; Al-Khedhairy, A.A. ZnO nanoparticles induces cell death in malignant human T98G gliomas, KB and non-malignant HEK cells. *J. Biomed. Nanotech.* **2013**, *9*, 1181–1189. [[CrossRef](#)]
11. Wahab, R.; Yang, Y.B.; Umar, A.; Singh, S.; Hwang, I.H.; Shin, H.S.; Kim, Y.S. Platinum quantum dots and their cytotoxic effect towards myoblast cancer cells (C2C12). *J. Biomed. Nanotech.* **2012**, *8*, 424–431. [[CrossRef](#)]
12. Cancer Incidence Report 2010. Saudi Arabia. Available online: www.scr.org.sa (accessed on 5 December 2021).

13. Galicia-Moreno, M.; Silva-Gomez, J.A.; Lucano-Landeros, S.; Santos, A.; Monroy-Ramirez, H.C.; Armendariz-Borunda, J. Liver Cancer: Therapeutic Challenges and the Importance of Experimental Models. *Can. J. Gastroenterol. Hepatol.* **2021**, *202*, 8837811. [[CrossRef](#)] [[PubMed](#)]
14. Sherman, M. Surveillance for hepatocellular carcinoma. *Semin. Oncol.* **2001**, *28*, 450–459. [[CrossRef](#)]
15. Ye, Q.H.; Qin, L.X.; Forgues, M.; He, P.; Kim, J.W.; Peng, A.C.; Simon, R.; Li, Y.; Robles, A.I.; Chen, Y.; et al. Predicting hepatitis B virus-positive metastatic hepatocellular carcinomas using gene expression profiling and supervised machine learning. *Nat. Med.* **2003**, *9*, 416–423. [[CrossRef](#)] [[PubMed](#)]
16. WHO. International Agency for Research in Cancer (IARC) Saudi Arabia. Source: Globocan. 2018. Available online: <https://gco.iarc.fr/today/data/factsheets/populations/682-saudi-arabia-fact-sheets.pdf> (accessed on 10 December 2018).
17. Saudi Arabia-Global Cancer Observatory. Available online: <https://gco.iarc.fr/today/data/factsheets/populations/682-saudi-arabia-fact-sheets.pdf> (accessed on 10 March 2021).
18. Pecorelli, S.; Favalli, G.; Zigliani, L.; Odicino, F. Cancer in women. *Int. J. Gynecol. Obstet.* **2003**, *82*, 369–379. [[CrossRef](#)]
19. Ferlay, J.; Parkin, D.M.; Steliarova-Foucher, E. Estimates of cancer incidence and mortality in Europe in 2008. *Eur. J. Cancer* **2010**, *46*, 765–781. [[CrossRef](#)] [[PubMed](#)]
20. Parkin, D.M.; Coleman, M.P. Changes in diet and changes in cancer risk: Observational studies. *IARC Sci. Publ.* **1990**, *103*, 93–111.
21. Sung, H.; Ferlay, J.; Siegel, R.L.; Laversanne, M.; Soerjomataram, I.; Jemal, A.; Bray, F. Global cancer statistics 2020: GLOBOCAN estimates of incidence and mortality worldwide for 36 cancers in 185 countries. *CA A Cancer J. Clin.* **2021**, *71*, 209–249. [[CrossRef](#)]
22. Nalwa, H.S.; Webster, T. (Eds.) *Cancer Nanotechnology-Nanomaterials for Cancer Diagnosis and Therapy*; American Scientific Publishers: Valencia, CA, USA, 2007.
23. White, M.G.; Schulte, J.J.; Xue, L.; Berger, Y.; Schuitevoerder, D.; Vining, C.C.; Kindler, H.L.; Husain, A.; Turaga, K.K.; Eng, O.S. Heterogeneity in PD-L1 expression in malignant peritoneal mesothelioma with systemic or intraperitoneal chemo therapy. *Br. J. Cancer* **2021**, *124*, 564–566. [[CrossRef](#)]
24. Boing, L.; Vieira, M.D.C.S.; Moratelli, J.; Bergmann, A.; Guimarães, A.C.D.A. Effects of exercise on physical outcomes of breast cancer survivors receiving hormone therapy—A systematic review and meta-analysis. *Maturitas* **2020**, *141*, 71–81. [[CrossRef](#)]
25. Chen, K.; Wei1, J.; Ge, C.; Xia, W.; Shi, Y.; Wang, H.; Jiang, X. Application of auto-planning in radiotherapy for breast cancer after breast-conserving surger. *Sci. Rep.* **2020**, *10*, 10927. [[CrossRef](#)] [[PubMed](#)]
26. Feng, B.; Niu, Z.; Hou, B.; Zhou, L.; Li, Y.; Yu, H. Enhancing Triple Negative Breast Cancer Immunotherapy by ICG-Templated Self-Assembly of Paclitaxel Nanoparticles. *Adv. Funct. Mater.* **2020**, *30*, 1906605. [[CrossRef](#)]
27. Sugidono, M.; Lo, M.; Young, R.; Rosario, K.; Jung, Y.; Huang, C.Y.; Sheng, Y.; Huang, L.W.; Olin, R.L. Impact of Polypharmacy Prior to Allogeneic Hematopoietic Stem Cell Transplantation in Older Adults. *Transplant. Cell. Ther.* **2021**, *27*, 344.e1–344.e5. [[CrossRef](#)] [[PubMed](#)]
28. Cammarata, F.P.; Forte, G.I.; Broggi, G.; Bravatà, V.; Minafra, L.; Pisciotta, P.; Calvaruso, M.; Tringali, R.; Tomasello, B.; Torrisi, F.; et al. Molecular Investigation on a Triple Negative BreastCancer Xenograft Model Exposed to Proton Beams. *Int. J. Mol. Sci.* **2020**, *21*, 6337. [[CrossRef](#)] [[PubMed](#)]
29. Rahmani, J.; Manzari, N.; Thompson, J.; Gudi, S.K.; Chhabra, M.; Naik, G.; Mousavi, S.M.; Varkaneh, H.K.; Clark, C.; Zhang, Y. The effect of metformin on biomarkers associated with breast cancer outcomes: A systematic review, meta-analysis, and dose-response of randomized clinical trials. *Clin. Transl. Oncol.* **2020**, *22*, 37–49. [[CrossRef](#)]
30. Snyder, K.K.; Buskirk, R.G.V.; Baust, J.G.; Baust, J.M. Breast Cancer Cryoablation: Assessment of the Impact of Fundamental Procedural Variables in an In Vitro Human Breast Cancer Model. *Breast Cancer Basic Clin. Res.* **2020**, *14*, 1–9. [[CrossRef](#)]
31. Wahab, R.; Dwivedi, S.; Umar, A.; Singh, S.; Hwang, I.H.; Shin, H.S.; Musarrat, J.; Al-Khedhairi, A.A.; Kim, Y.S. ZnO Nanoparticles Induce Oxidative Stress in Cloudman S91 Melanoma Cancer Cells. *J. Biomed. Nanotech.* **2013**, *9*, 441–449. [[CrossRef](#)]
32. Nguyen, L.N.; Kaushik, N.; Lamichhane, P.; Mumtaz, S.; Paneru, R.; Bhartiya, P.; Kwon, J.S.; Mishra, Y.K.; Nguyen, L.Q.; Kaushik, N.K.; et al. In situ plasma-assisted synthesis of polydopamine-functionalized gold nanoparticles for biomedical applications. *Green Chem.* **2020**, *22*, 6588–6599. [[CrossRef](#)]
33. Bendale, Y.; Bendale, V.; Paul, S. Evaluation of cytotoxic activity of platinum nanoparticles against normal and cancer cells and its anticancer potential through induction of apoptosis. *Integr. Med. Res.* **2017**, *6*, 141–148. [[CrossRef](#)]
34. Khorshid, F.A.; Raouf, G.A.; El-Hamidy, S.M.; Al-amri, G.S.; Alotaibi, N.A.; Kumosani, T.A. PMF, Cesium & Rubidium Nanoparticles Induce Apoptosis in A549 Cells. *Life Sci. J.* **2011**, *8*, 534–542.
35. Nayak, V.; Singh, K.R.B.; Singh, A.K.; Singh, R.P. Potentialities of selenium nanoparticles in biomedical science. *New J. Chem.* **2021**, *45*, 2849–2878. [[CrossRef](#)]
36. Mavaei, M.; Chahardoli, A.; Shokoohinia, Y.; Khoshroo, A.; Fattahi, A. One-step Synthesized Silver Nanoparticles Using Isoimperatorin: Evaluation of Photocatalytic, and Electrochemical Activities. *Sci. Rep.* **2020**, *10*, 1762. [[CrossRef](#)] [[PubMed](#)]
37. Kolya, H.; Kuila, T.; Kim, N.H.; Lee, J.H. Bioinspired silver nanoparticles/reduced graphene oxide nanocomposites for catalytic reduction of 4-nitrophenol, organic dyes and act as energy storage electrode material. *Compos. Part B Eng.* **2019**, *173*, 106924. [[CrossRef](#)]
38. Molina, G.; Murcia, S.; Molera, J.; Roldan, C.; Crespo, D.; Pradell, T. Color and dichroism of silver-stained glasses. *J. Nanoparticle Res.* **2013**, *15*, 1932. [[CrossRef](#)]
39. Lv, Y.; Liu, H.; Wang, Z.; Liu, S.; Hao, L.; Sang, Y.; Liu, D.; Wang, J.; Boughton, R.I. Silver nanoparticle-decorated porous ceramic composite for water treatment. *J. Membr. Sci.* **2009**, *331*, 50–56. [[CrossRef](#)]

40. Guo, H.; Zhang, Z.; Xing, B.; Mukherjee, A.; Musante, C.; White, J.C.; He, L. Analysis of Silver Nanoparticles in Antimicrobial Products Using Surface-Enhanced Raman Spectroscopy (SERS). *Environ. Sci. Technol.* **2015**, *49*, 4317–4324. [[CrossRef](#)]
41. Austin, L.A.; Mackey, M.A.; Dreaden, E.C.; El-Sayed, M.A. The optical, photothermal, and facile surface chemical properties of gold and silver nanoparticles in bionanotechnology, therapy, and drug delivery. *Arch. Toxicol.* **2014**, *88*, 1391–1417. [[CrossRef](#)]
42. Austin, L.A.; Kang, B.; Yen, C.W.; El-Sayed, M.A. Plasmonic Imaging of Human Oral Cancer Cell Communities during Programmed Cell Death by Nuclear-Targeting Silver Nanoparticles. *J. Am. Chem. Soc.* **2011**, *133*, 17594–17597. [[CrossRef](#)] [[PubMed](#)]
43. Gopinath, P.; Gogoi, S.K.; Chattopadhyay, A.; Ghosh, S.S. Implications of silver nanoparticle induced cell apoptosis for in vitro gene therapy. *Nanotechnology* **2008**, *19*, 075104. [[CrossRef](#)]
44. Kalpana, D.; Han, J.H.; Park, W.S.; Lee, S.M.; Wahab, R.; Lee, Y.S. Green biosynthesis of silver nanoparticles using *Torreya nucifera* and their antibacterial activity. *Arab. J. Chem.* **2019**, *12*, 1722–1732. [[CrossRef](#)]
45. Rai, M.; Yadav, A.; Gade, A. Silver nanoparticles as a new generation of anti microbials. *Biotechnol. Adv.* **2009**, *27*, 76–83. [[CrossRef](#)] [[PubMed](#)]
46. Dakal, T.C.; Kumar, A.; Majumdar, R.S.; Yadav, V. Mechanistic basis of antimicrobial actions of silver nanoparticles. *Front. Microbiol.* **2016**, *16*, 1831. [[CrossRef](#)]
47. Buttacavoli, M.; Albanese, N.N.; Di, C.G.; Alduina, R.; Faleri, C.; Gallo, M.; Pizzolanti, G.; Gallo, G.; Feo, S.; Baldi, F.; et al. Anticancer activity of biogenerated silver nanoparticles: An integrated proteomic investigation. *Oncotarget* **2018**, *9*, 9685–9705. [[CrossRef](#)] [[PubMed](#)]
48. Bastús, G.N.; Merkoçi, F.; Piella, J.; Puentes, V. Synthesis of Highly Monodisperse Citrate-Stabilized Silver Nanoparticles of up to 200 nm: Kinetic Control and Catalytic Properties. *Chem. Mater.* **2014**, *26*, 2836–2846. [[CrossRef](#)]
49. Alshehri, A.H.; Jakubowska, M.; Młozniak, A.; Horaczek, M.; Rudka, D.; Free, C.; Carey, J.D. Enhanced Electrical Conductivity of Silver Nanoparticles for High Frequency Electronic Applications. *ACS Appl. Mater. Interfaces* **2012**, *4*, 7007–7010. [[CrossRef](#)]
50. Ahamed, M.; Akhtar, M.J.; Khan, M.A.; Alhadlaq, H.A. Novel Green Preparation of Ag/RGO Nanocomposites with Highly Effective Anticancer Performance. *Polymers* **2021**, *13*, 3350. [[CrossRef](#)]
51. Ahamed, M.; Akhtar, M.J.; Khan, M.M.; Alhadlaq, H.A. SnO₂-Doped ZnO/Reduced Graphene Oxide Nanocomposites: Synthesis, Characterization, and Improved Anticancer Activity via Oxidative Stress Pathway. *Int. J. Nanomed.* **2021**, *16*, 89–104. [[CrossRef](#)]
52. Jebiril, S.; Jenana, R.K.B.; Dridi, C. Green synthesis of silver nanoparticles using *Melia azedarach* leaf extract and their antifungal activities: In vitro and in vivo. *Mater. Chem. Phys.* **2020**, *248*, 122898. [[CrossRef](#)]
53. Skiba, M.I.; Vorobyova, V.I.; Pivovarov, A.; Makarshenko, N.P. Green Synthesis of Silver Nanoparticles in the Presence of Polysaccharide: Optimization and Characterization. *J. Nanomater.* **2020**, *2020*, 3051308. [[CrossRef](#)]
54. Hamida, R.S.; Albasher, G.; Bin-Meferij, M.M. Oxidative Stress and Apoptotic Responses Elicited by Nostoc-Synthesized Silver Nanoparticles against Different Cancer Cell Lines. *Cancers* **2020**, *12*, 2099. [[CrossRef](#)]
55. Priya, K.; Vijayakumar, M.; Janani, B. Chitosan-mediated synthesis of biogenic silver nanoparticles (AgNPs), nanoparticle characterisation and in vitro assessment of anticancer activity in human hepatocellular carcinoma HepG2 cells. *Inter. J. Biol. Macromol.* **2020**, *149*, 844–852. [[CrossRef](#)]
56. Siddiqui, M.A.; Singh, G.; Kashyap, M.P.; Khanna, V.K.; Yadav, S.; Chandra, D.; Pant, A.B. Influence of cytotoxic doses of 4-hydroxynonenal on selected neuro transmitter receptors in PC-12 cells. *Toxicol. In Vitro* **2008**, *22*, 1681–1688. [[CrossRef](#)]
57. Wahab, R.; Siddiqui, M.A.; Saquib, Q.; Dwivedi, S.; Ahmad, J.; Musarrat, J.; Al-Khedhairi, A.A.; Shin, H.S. ZnO nanoparticles induced oxidative stress and apoptosis in HepG2 and MCF-7 cancer cells and their antibacterial activity. *Colloids Surf. B Biointerfaces* **2014**, *117*, 267–276. [[CrossRef](#)]
58. Alkhdhayri, A.A.; Wahab, R.; Siddiqui, M.A.; Ahmad, J. Selenium nanoparticles induce cytotoxicity and apoptosis in human breast cancer (MCF-7) and liver (HEPG2) cell lines. *Nanosci. Nanotechnol. Lett.* **2020**, *12*, 324–330. [[CrossRef](#)]
59. Mosmann, T. Rapid colorimetric assay for cellular growth and survival: Application to proliferation and cytotoxicity assays. *J. Immunol. Methods* **1983**, *65*, 55–63. [[CrossRef](#)]
60. Borenfreund, E.; Puerner, J.A. Toxicity determined in vitro by morphological alterations and neutral red absorption. *Toxicol. Lett.* **1985**, *24*, 119–124. [[CrossRef](#)]
61. Siddiqui, M.A.; Kashyap, M.P.; Kumar, V.; Al-Khedhairi, A.A.; Musarrat, J.; Pant, A.B. Protective potential of trans-resveratrol against 4-hydroxynonenal induced damage in PC12 cells. *Toxicol. Vitro* **2010**, *24*, 1592–1598. [[CrossRef](#)] [[PubMed](#)]
62. Zhao, J.; Riediker, M. Detecting the oxidative reactivity of nanoparticles: A new protocol for reducing artifacts. *J. Nanopart. Res.* **2014**, *16*, 2493. [[CrossRef](#)] [[PubMed](#)]
63. Davis, K.; Yarbrough, R.; Froeschle, M.; White, J.; Rathnayake, H. Band gap engineered zinc oxide nanostructures via a sol-gel synthesis of solvent driven shape controlled crystal growth. *RSC Adv.* **2019**, *9*, 14638–14648. [[CrossRef](#)]
64. Steinmetz, L.; Geers, C.; Balog, S.; Bonmarin, M.; Rodriguez-Lorenzo, L.; Taladriz-Blanco, P.; Rothen-Rutishauser, B.; Petri-Fink, A. A comparative study of silver nanoparticle dissolution under physiological conditions. *Nanoscale Adv.* **2020**, *2*, 5760–5768. [[CrossRef](#)]
65. Khan, I.; Saeed, K.; Khan, I. Nanoparticles: Properties, applications and toxicities. *Arab. J. Chem.* **2019**, *12*, 908–931. [[CrossRef](#)]
66. Vismara, E.; Valerio, A.; Coletti, A.; Torri, G.; Bertini, S.; Eisele, G.; Gornati, R.; Bernardini, G. Non-Covalent Synthesis of Metal Oxide Nanoparticle-Heparin Hybrid Systems: A New Approach to Bioactive Nanoparticles. *Int. J. Mol. Sci.* **2013**, *14*, 13463–13481. [[CrossRef](#)]

67. Kumari, M.; Mukherjee, A.; Chandrasekaran, N. Genotoxicity of silver nanoparticles in *Allium cepa*. *Sci. Total Environ.* **2009**, *407*, 5243–5246. [[CrossRef](#)]
68. Wahab, R.; Dwivedi, S.; Khan, F.; Mishra, Y.K.; Hwang, I.H.; Shin, H.S.; Musarrat, J.; Al-Khedhairi, A.A. Statistical analysis of gold nanoparticle-induced oxidative stress and apoptosis in myoblast (C2C12) cells. *Colloids Surf. B Biointerfaces* **2014**, *123*, 664–672. [[CrossRef](#)] [[PubMed](#)]
69. Bahadar, H.; Maqbool, F.; Niaz, K.; Abdollahi, M. Toxicity of nanoparticles and an overview of current experimental models. *Iran. Biomed. J.* **2016**, *20*, 1–11. [[PubMed](#)]
70. Sohaebuddin, S.K.; Thevenot, P.T.; Baker, D.; Eaton, J.W.; Tang, L. Nanomaterial cytotoxicity is composition, size, and cell type dependent. *Part. Fibre Toxicol.* **2010**, *7*, 22. [[CrossRef](#)]
71. Pujalté, I.; Passagne, I.; Brouillaud, B.; Tréguer, M.; Durand, E.; Courtès, C.O.; L'Azou, B. Cytotoxicity and oxidative stress induced by different metallic nanoparticles on human kidney cells. *Part. Fibre Toxicol.* **2011**, *8*, 10. [[CrossRef](#)]
72. Ahmed, K.B.R.; Nagy, A.M.; Brown, R.P.; Zhang, Q.; Malghan, S.G.; Goering, P.L. Silver nanoparticles: Significance of physico-chemical properties and assay interference on the interpretation of in vitro cytotoxicity studies. *Toxicol. Vitro.* **2017**, *38*, 179–192. [[CrossRef](#)]
73. Pablo, F.P.; Guy, S.S. The protein structures that shape caspase activity, specificity, activation and inhibition. *Biochem. J.* **2004**, *384*, 201–232.
74. Youle, R.J.; Strasser, A. The BCL-2 protein family: Opposing activities that mediate cell death. *Nat. Rev. Mol. Cell Biol.* **2008**, *9*, 47–59. [[CrossRef](#)]
75. Limbach, L.K.; Li, Y.; Grass, R.N.; Brunner, T.J.; Hintermann, M.A.; Muller, M.; Gunther, D.; Stark, W.J. Oxide Nanoparticle Uptake in Human Lung Fibroblasts: Effects of Particle Size, Agglomeration, and Diffusion at Low Concentrations. *Environ. Sci. Technol.* **2005**, *39*, 9370. [[CrossRef](#)] [[PubMed](#)]
76. Jeng, H.A.; Swanson, J. Toxicity of Metal Oxide Nanoparticles in Mammalian Cells. *J. Environ. Sci. Health Part A* **2006**, *41*, 2699–2711. [[CrossRef](#)] [[PubMed](#)]